Chapter-3

Dynamical Conductivity

of

High-T_c Superconductors Below T_c

CHAPTER-III

DYNAMICAL CONDUCTIVITY OF HIGH-T_c SUPERCONDUCTORS BELOW T_c

In this chapter, we present a model calculation of frequency and temperature dependent conductivity for temperatures below T_c. Calculation has been performed for cuprate superconductors with one and two conducting Cu-O layers per unit cell. However, our results are mainly discussed for YBCO which consists of two conducting layers per unit cell. To make a comparison between our calculations and experimental results, we introduced frequency and temperature dependent transport relaxation time and frequency dependent effective mass of electron in our calculation. Our computed macroscopic conductivity as a function of temperature in microwave frequency regime shows a very good agreement with experimental data. A good agreement between our calculated macroscopic conductivity as a function of frequency and experimental results has also been obtained. It is found that the peak in temperature dependent conductivity, in microwave regime, is the manifestation of temperature and frequency dependent transport relaxation time. Our calculation of microscopic conductivity gives the frequency of longitudinal collective excitation modes whose frequency, for an arbitrary value of wave vector, lies below the frequency gap. These observations are very similar to those reported prior by Fertig and Das Sarma.

3.1 INTRODUCTION

Dynamical conductivity of cuprate superconductors (CS) in different frequency(ω) and temperature(T) regimes has been a subject of imance interest, during past few years. Several experimental [1-9] as well as theoretical [10-17] studied have been performed on infra-red as well as microwave conductivity of CS above and below T_c. Recent, experimental studies on c-axis transport in CS have attracted a great deal of interest [3,18,19]. Most of the CS are layered materials in which layers are weakly coupled along c-axis. Nature of c-axis dynamical conductivity differs dramatically from that of a-b plane dynamical conductivity. It has widely been acknowledged that the mechanism of charge transport along c-axis must be fundamentally different from the mechanism of charge transport in a-b plane. Most interesting part of the studies on c-axis ω-dependent conductivity is the appearance of pseudogap (a gap like depression) in it. Several explanation have been put forward for pseudogap in c-axis ω-dependent conductivity. Angle-resolved photoemission and time-resolved optical photomodulation data on underdoped CS suggest that some kind of gap may also be present (at least for parts of Fermi-surface) for charge excitations. The appearance of such a pseudogap above T_c appears to be a general phenomena in all CS. The pseudogap state of the underdoped CS represents some type of pairing above T_c which has been postulated to derived from nuclear spinon pairs [20], spin density wave states [21], or from some form of (2e) Cooper pairing which foreshadows the ultimate superconducting state. The a-b plane optical data have mainly been discussed within the frame-work of extended Drude model with ω-and T-dependent transport scattering rate $\tau(\omega, T)$ and the mass of a charge carrier. The a-b plane optical data on optimally doped CS reals that the real part of optical conductivity in low frequency regime ($\omega \leq 50$ meV) exhibits ($1/\omega$)-dependence rather than ($1/\omega^2$)-dependence behavior

of Fermi-liquid. There appears to be a crossing point in optical conductivity of different doping concentration at special ω-value.

An analysis of a-b plane optical conductivity data on CS has also been presented in terms of two component picture of charge carriers rather than the opening of a simple gap for charge carrier excitation below a well defined temperature. It has been shown that an analysis of a-b plane optical conductivity as a function of T and doping suggests that a dip in spectrum which separates the infra-red charge excitation spectrum into two components with distinct energy scales. The interpretation is found to be consistent with angle-resolved photoemission and electronic Raman spectra.

Recent measurements on a-b plane microwave and infra-red conductivity as a function of T below T_c exhibit peak in real part of conductivity. The peak is broad and it increases in magnitude and shifts to lower T-values on decreasing ω. This peak has widely been interpreted to be due to the rapid reduction in the inelastic scattering rate below T_c [13]. It is envisaged that a gap opens up in the spectral density of underlying fluctuation spectrum, which is responsible for drastic reduction of scattering rate below T_c, as compared to the value above T_c. The scattering rate above T_c in CS depends almost linearly on T for $\omega \rightarrow 0$ and it also exhibits linear ω-dependence for $\omega \gg T$. The scattering above T_c in CS has been found much larger than that in conventional superconductors.

The aim of this chapter is to explain some or the features of the experimental data on ω-and T-dependent dynamical conductivity of CS below T_c, using a simple model. A CS has seen modeled to be layered structure of Cu-O conducting layer (COCL) embedded into an anisotropic dielectric medium of back ground dielectric function, $\varepsilon_{ab}(\omega)$ along a-b plane and $\varepsilon_c(\omega)$ along

63

c-axis. The $\varepsilon_{ab}(\omega)$ and $\varepsilon_c(\omega)$ are expressed in a phenomenological manner in terms of a phonon frequencies. A coupling between the COCL is taken into consideration for calculating polarization function of a COCL. Further, ω-and T-dependence of $\tau(\omega, T)$ is taken in a phenomenological manner and nature of ω-and T-dependent $\tau(\omega, T)$ has been chosen to be same for both the cases of $T \geq T_c$ and $T < T_c$. Also, ω-dependence of effective mass of an electron has been introduced in our model calculation, in order to obtain good agreement between our calculation and available experimental data. The formalism used and the calculations are reported in sec. 3.2. Our results along with experimental data are discussed in sec. 3.3. We also performed a calculation of macroscopic and microscopic dynamical conductivity just below T_c, using polarization function given by Sharma and Kulshrestha [31] to study collective excitations in superconducting superlattices. This calculation is reported in sec. 3.4.

3.2 FORMALISM AND CALCULATION

As is mentioned in chapter-II, response of a system to an electromagnetic field can be described in terms of Maxwell's equation. Response of a longitudinal external field to a CS is described by Eq. (2.1). In this chapter, we confined to the response of CS to longitudinal field in long wavelength limit.

$$\sigma(\mathbf{r}, \mathbf{r}', \omega) = \int \varepsilon^{-1}(\mathbf{r}, \mathbf{r}'', \omega) \sigma^0(\mathbf{r}'', \mathbf{r}', \omega) \, d^3 r'', \tag{3.1}$$

where $\sigma(\mathbf{r}, \mathbf{r}', \omega)$ and $\sigma^0(\mathbf{r}, \mathbf{r}', \omega)$ are microscopic conductivity and macroscopic conductivity, respectively at frequency, ω. $\varepsilon^{-1}(\mathbf{r}, \mathbf{r}', \omega)$ is the inverse of dielectric response function of $\varepsilon(\mathbf{r}, \mathbf{r}', \omega)$ which is given by

$$\varepsilon(\mathbf{r}, \mathbf{r}', \omega) = \varepsilon_l(\omega) \, \delta(\mathbf{r} - \mathbf{r}') - \int \Pi(\mathbf{r}, \mathbf{r}', \omega) \, v(\mathbf{r}'', \mathbf{r}') \, d^3 r'', \tag{3.2}$$

where $\Pi(\mathbf{r}, \mathbf{r}', \omega)$ is the polarization function in the absence of bare Coulomb electron-electron interaction

$$v(\mathbf{r}, \mathbf{r}') = \frac{e^2}{|\mathbf{r} - \mathbf{r}'|} \qquad (3.3)$$

The $\varepsilon_l(\omega)$ represents $\varepsilon_{ab}(\omega)$ for interaction confined to a-b plane and it represents $\varepsilon_c(\omega)$ for interaction along c-axis. As was mentioned in chapter-II, existing theoretical and experimental investigations on lattice vibrations in CS suggest that there exist several optical and acoustical phonon branches both along a-b plane as well as along c-axis [22]. Again, number of phonon branches and their frequencies along a-b plane differ from those along c-axis. A phenomenological expression for $\varepsilon_l(\omega)$ is given by Eq. (2.7). For the sake of completeness, we rewrite Eq. (2.7) below,

$$\varepsilon_l(\omega) = \{\varepsilon_\infty / l\} \sum_{i=1}^{l} \frac{[\omega_{Li}^2 - \omega(\omega + i\gamma_{ph})]}{[\omega_{Ti}^2 - \omega(\omega + i\gamma_{ph})]} . \qquad (3.4)$$

The ε_∞ and l are high frequency dielectric constant and number of phonon branches, respectively. The ω_{Li} (ω_{Ti}) is the frequency of the phonon branches. γ_{ph} is damping constant for lattice vibrations, which is chosen to be same for all phonon branches. We choose a-b plane along x-y plane and c-axis along z-axis to Fourier transform Eq. (3.1). We obtain

$$\sigma_p(q, k_z, \omega, T) = \frac{\sigma^0_p(q, k_z, \omega, T)}{\varepsilon_p(q, k_z, \omega, T)} , \qquad (3.5)$$

65

where q and k_z are wave vector components along a-b plane and c-axis, respectively. The subscript ρ represents number of COCL in a unit cell. For a CS consisting of one COCL per unit cell, we can write

$$\sigma^0_1(q, k_z, \omega, T) = \{-i\omega / 4\pi\}[\varepsilon_1(q, k_z, \omega, T) - 1] \qquad (3.6)$$

To proceed further, we have to specify the nature of interaction between the layers. In case of CS, width of a layer consisting of charge carriers is much smaller as compared with separation between two adjusting layers. Therefore the possible coupling between the layers should be weak, which could allow a small charge transfer between the layers. For a weak coupling case, $\varepsilon_1(q, k_z, \omega, T)$ is given by [23]

$$\varepsilon_1(q, k_z, \omega, T) = \varepsilon_l(\omega) - \{2\pi e^2 d/q\} \, \Pi(q, k_z, \omega, T)S(q, k_z), \qquad (3.7)$$

where d is length of a unit cell along c-axis. The structure factor is defined as

$$S(q, k_z) = \frac{\sinh(qd)}{\cosh(qd) - \cos(k_z d)} \qquad (3.8)$$

For CS having two COCL per unit cell, we obtain
$$\sigma^0_2(q, k_z, \omega, T) =$$
$$\sigma^0_1(q, k_z, \omega, T)[2-\{2\pi e^2 d/q\varepsilon_l(\omega)\}\Pi(q, k_z, \omega, T)\{2S(q, k_z) - S'(q, k_z) - S''(q, k_z)\}]$$

$$(3.9)$$

$$\varepsilon_2(q, k_z, \omega, T) = \varepsilon_l(\omega) - [\{4\pi e^2 d/q\}\Pi(q, k_z, \omega, T)S(q, k_z)]$$
$$+ [\{2\pi e^2 d/q\}^2/\varepsilon_l(\omega)]\Pi^2(q, k_z, \omega, T)\{S^2(q, k_z) - S'(q, k_z) S''(q, k_z)\}$$

$$(3.10)$$

66

The $S'(q, k_z)$ and $S''(q, k_z)$ are complex conjugate of each other and $S'(q, k_z)$ is defined by

$$S'(q, k_z) = \frac{\sinh(qd') + \exp(-ik_z d)\sinh(qd_1)}{\cosh(qd) - \cos(k_z d)} \qquad (3.11)$$

where $d' = d - d_1$, d_1 is separation between two COCLs in a unit cell of CS consisting of two COCL per unit cell. Eqs. (3.5) to (3.11) describe dynamical conductivity of a CS for all values of q, k_z, ω and T.

3.3 CONDUCTIVITY WITH WEEK CHARGE TRANSFER BETWEEN CONDUCTING LAYERS

Further evaluation of $\sigma^0_\rho(q, k_z, \omega, T)$ and $\sigma_\rho(q, k_z, \omega, T)$ depends on calculation of $\Pi(q, k_z, \omega, T)$. Our aim is to perform a model calculation which incorporates basic characteristics of CS in a simple manner. For the case of weak coupling between COCls in long wave length limit, $\Pi(q, k_z, \omega, T)$ can be given by [24,25]

$$\Pi(q, k_z, \omega, T) = \frac{\{nq^2/m^*\}[1 + \{4\omega_g^2 \sin^2(k_z d/2)/ \omega_P^2 (qd)^2\}] [X_s + X_s(\omega / \omega + i\gamma_n)]}{A(q, k_z) - \omega(\omega + i\gamma_s)}$$

$$(3.12)$$

with

$$A(q, k_z) = \frac{qv_F^2}{dS(q, k_z)} [1 + \frac{m^* v_0}{2\pi h^2}] \qquad (3.13)$$

where $\omega_p = \{4\pi n e^2/m^*\}^{1/2}$ is usual plasma frequency. n is number of electron per unit volume. $X_s (= n_s/n)$ and $X_n (= n_n/n)$ are superfluid and normal fluid fractions, respectively. γ_n and γ_s are inverse of scattering rate of normal and superconducting state, respectively. v_F is 2D Fermi velocity. v_0 is attractive potential within a layer and m^* is effective mass of an electron. ω_g is measure of coupling between COCLs. It depends on overlap integral between two adjacent COCLs, length of a unit cell and the effective Bohr radius [25]. The ω_g does not appear in single particle energy but it appears in $\Pi(q, k_z, \omega, T)$. Therefore it represents a kind of pseudogap whose presence in single particle excitation across Fermi surface has been suggested by recent angle-resolved photoemission and time-resolved optical modulation experiments [26,27].

Recent experiments on the measurements of surface resistance and optical properties of CS suggest that quasi-particle transport scattering rate, for both the cases of $T > T_c$ and $T < T_c$, depends on ω and T. Further it has been found that T-dependence of $\tau(\omega, T)$ for $T >> \omega$ is almost identical to the ω-dependence of $\tau(\omega, T)$ for $\omega >> T$. However, h/τ is rapidly suppressed on decreasing T form above T_c to below T_c [13]. A simple expression which describes ω and T dependence of $\gamma_{n/s}$ reasonably well, can be given by [28]

$$\gamma_{n/s}(\omega, T) = \alpha_{n/s} [\beta^2_{n/s} T^2 + \omega^2]^{1/2} \qquad (3.14)$$

where $\alpha_{n/s}$ and $\beta_{n/s}$ are constants which involve electron-electron interaction in a CS. The α_s is much smaller α_n because of rapid suppression of scattering processes below T_c. Further, we express α_s as a function of $\omega \leq \omega_c$, where ω_c is the cut-off frequency [28]. The T-dependence of X_s (= $1-X_n$) used in Eq. (3.12), is determined form experimental data on T-dependent penetration depth, $\lambda(T)$.

The $X_s = \lambda^2(0)/\lambda^2(T)$ has been used to deduce X_s from experimental data $\lambda^2(0)/\lambda^2(T)$ versus T, using numerical method of polynomial interpolation.

3.3.1 RESULTS AND DISCUSSION

Main results of our calculation are given by Eqs. (3.5) to (3.12). Major part of our discussion is devoted to CS with two COCL per unit cell. We apply our calculation to $YBa_2Cu_3O_{7-\delta}$ (YBCO) for which maximum experimental data is available in the existing literature. We divide this section into two parts. Macroscopic conductivity is discussed in first part, whereas discussion on microscopic conductivity are reported in second part.

3.3.1(a) Macroscopic Conductivity

The YBCO is modeled in terms of following values of parameter: $\varepsilon_\infty = 4.0$, $d = 11.67$ A^0, $d_1 = d/3$ and $n = 17 \times 10^{21}$ cm^{-3}. m^*, which is used to compute ω_p defined above, in general is ω-and T-dependent. Also, it has larger value in superconducting state as compared to that in normal state. We define $m^* = f(\omega)m_e$, where m_e is a function of ω. The ω-dependence of $f(\omega)$ will be discuss later. There exist several phonon branches in YBCO. However to compute dominant ω-dependent behavior of $\varepsilon_i(\omega)$ in a simple manner, we incorporated contribution from optical phonons only. To compute $\varepsilon_{ab}(\omega)$, we took four optical phonon branches; $\omega_{L1} = 67.48$ meV, $\omega_{L2} = 58.25$ meV, $\omega_{L3} = 42.38$ meV, $\omega_{L4} = 29.62$ meV, $\omega_{T1} = 67.42$ meV, $\omega_{T2} = 48.96$ meV, $\omega_{T3} = 35.94$ meV and $\omega_{T4} = 29.50$ meV [22]. The frequency of three optical phonon branches which mainly contributes to $\varepsilon_c(\omega)$ are as; $\omega_{L1} = 52.43$ meV, $\omega_{L2} = 25.78$ meV, $\omega_{L3} = 18.59$ meV, $\omega_{T1} = 46.48$ meV, $\omega_{T2} = 19.95$ meV, $\omega_{T3} = 13.50$ meV [22]. As has been mentioned before, $\alpha_s \ll \alpha_n$ and β_s differs from β_n because of rapid suppression

below T_c. The ω-dependence of $\alpha_s(\omega)$ has been determined by keeping in mind; (i) almost linear ω-dependence of γ_s and (ii) to obtain a best possible agreement between our calculation and experimental results on macroscopic conductivity. Existing theoretical and experimental work on $\gamma_s(\omega)$ suggests that $\gamma_s(\omega)$ almost linearly depends on ω for all values of ω, covering microwave to optical frequency regime.

Our interpolated values of X_s along *a-b* plane using experimental data on $\lambda^2(0)/\lambda^2(T)$ from Ref. 3 are plotted as a function of T/T_c in Fig. 3.1. The interpolation has been done using Langrange's formula with Pade approximation for rational function interpolation (Fortran programme used for interpolation is given in the Appendix). As can be seen from the figure, T-dependent of X_s along *a-b* plane is different from that along *c*-axis. In order to compare our theoretical results with available experimental data, we computed $Re\sigma_2^0(q, k_z, \omega, T)$ (real part of $\sigma_2^0(q, k_z, \omega, T)$) as a function of T for three values of ω for fixed qd and k_zd and then as a function of ω for fixed T, qd and k_zd. To compute $Re\sigma_2^0(q, k_z, \omega, T)$ using Eq. (3.9) and (3.12), we require γ_n, γ_s, X_s and v_0, as is obvious from Eq.(3.12) and (3.13). As has been mentioned before, in order to obtain a good agreement between our calculation and experimental results, α_s and m^* are to be taken ω-dependent. Keeping in mind the behavior of α_s and m^* as a function of ω deduced from experimental data on dynamical conductivity, it has been suggested that α_s and m^* depend on ω for $\omega \leq \omega_c$, where ω_c is a cut-off frequency [28]. For computation of our results we have taken $\omega_c = 0.15$ meV for YBCO. For $\omega > \omega_c$, α_s and m^* are taken to be independent of ω. We used $\alpha_s = 0.0045$ and $m^*/m_e = 2.0$ for $\omega > 0.15$ meV. To choose the ω-dependence of α_s and m^* for $\omega \leq 0.15$ meV, our guiding principle has been a best possible agreement between our calculation and the available experimental results on microwave dynamical conductivity. Our computed
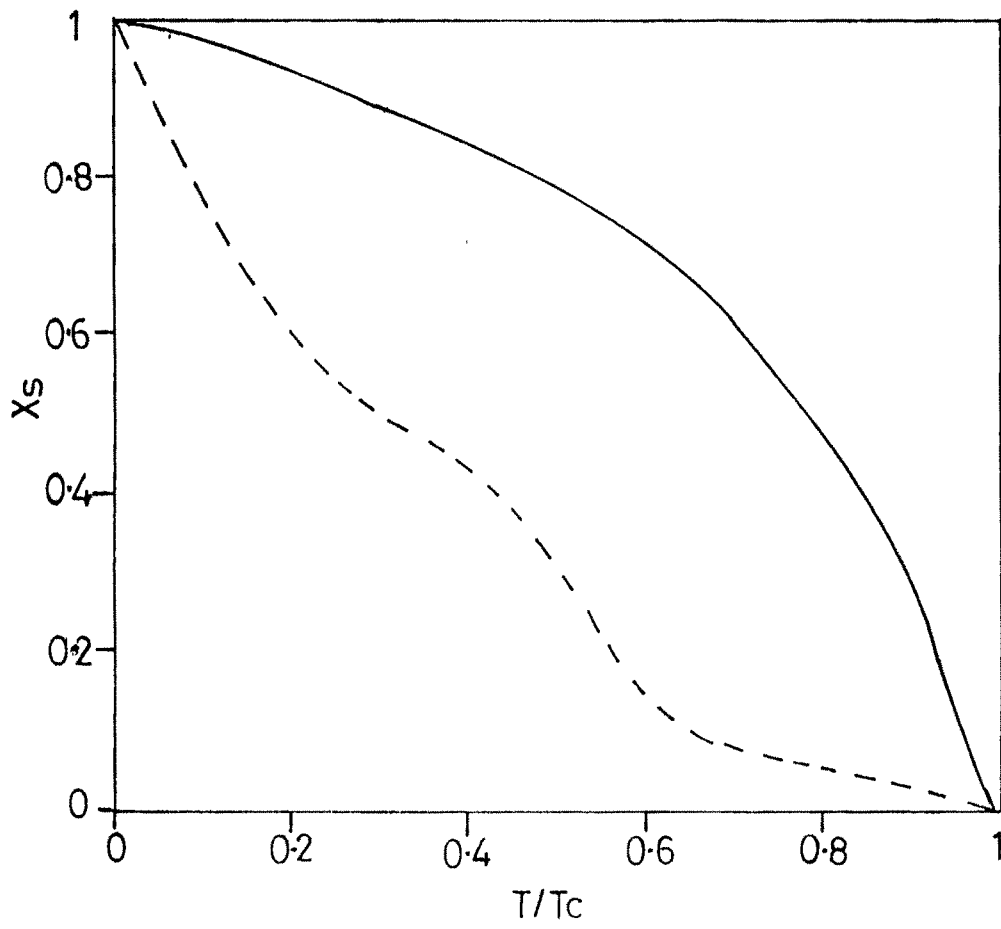
Fig. 3.1 Plot of interpolated X_s $\{=\lambda^2(0)/\lambda^2(T)\}$ versus T/T_c for *a-b* plane (solid line curve) and for *c*-axis(desh-desh line curve)

$\alpha_s^{ab}(\omega)$ and m^*/m_e for *a-b* plane conduction are plotted as a function of ω in Fig. 3.2. It can be seen from the figure that m^*/m_e has a strong ω-dependence for $\omega < 0.02$ meV and it becomes almost independent of ω for ω close to 0.15 meV. The plotted m^*/m_e versus ω can be fitted to an interpolated polynomial of degree six. We find that

$$m^*/m_e = 0.580464 \times 10^2 - 0.304771 \times 10^4 \omega + 0.943226 \times 10^5 \omega^2 - 0.153507 \times 10^7 \omega^3$$
$$+ 0.135645 \times 10^8 \omega^4 - 0.619095 \times 10^8 \omega^5 + 0.114341 \times 10^9 \omega^6$$

$$(3.15)$$

for $\omega \leq 0.15$ meV. The computed α_s versus ω becomes almost independent of ω approaching to 0.15 meV as can be seen from the figure. Interpolated polynomial which fits the α_s versus ω curve is given by

$$\alpha_s^{ab} = 0.361835 \times 10^{-4} + 0.566579 \times 10^{-1} \omega - 0.186080 \ \omega^2 + 0.174238 \ \omega^3$$
$$- 0.142348 \times 10^1 \omega^4 + 0.413868 \times 10^1 \omega^5$$

$$(3.16)$$

Our computed $\gamma_s(\omega)$ as a function of ω for different T-values (for T<T$_c$) is plotted in Fig. 3.3. As can be seen be from the figure $\gamma_s(\omega, T)$ depends almost linearly on ω for different value of T. The behavior of our computed $\gamma_s(\omega, T)$ shown in Fig. 3.3 agrees with the behavior of $\gamma_s(\omega, T)$ deduced from the experimental data on dynamical conductivity [2-4].

Our computed $Re\sigma^0_{2ab}(q, \omega, T)$, value of $Re\sigma^0_2(q, k_z, \omega, T)$ for *a-b* plane, is plotted as a function of T for three values of ω (0.0122 meV, 0.0397 meV, 0.144 meV) and qd$\rightarrow$0 in Fig. 3.4. The experimental data [2-4] has also been plotted in figure along with the theoretical results. For computation of our
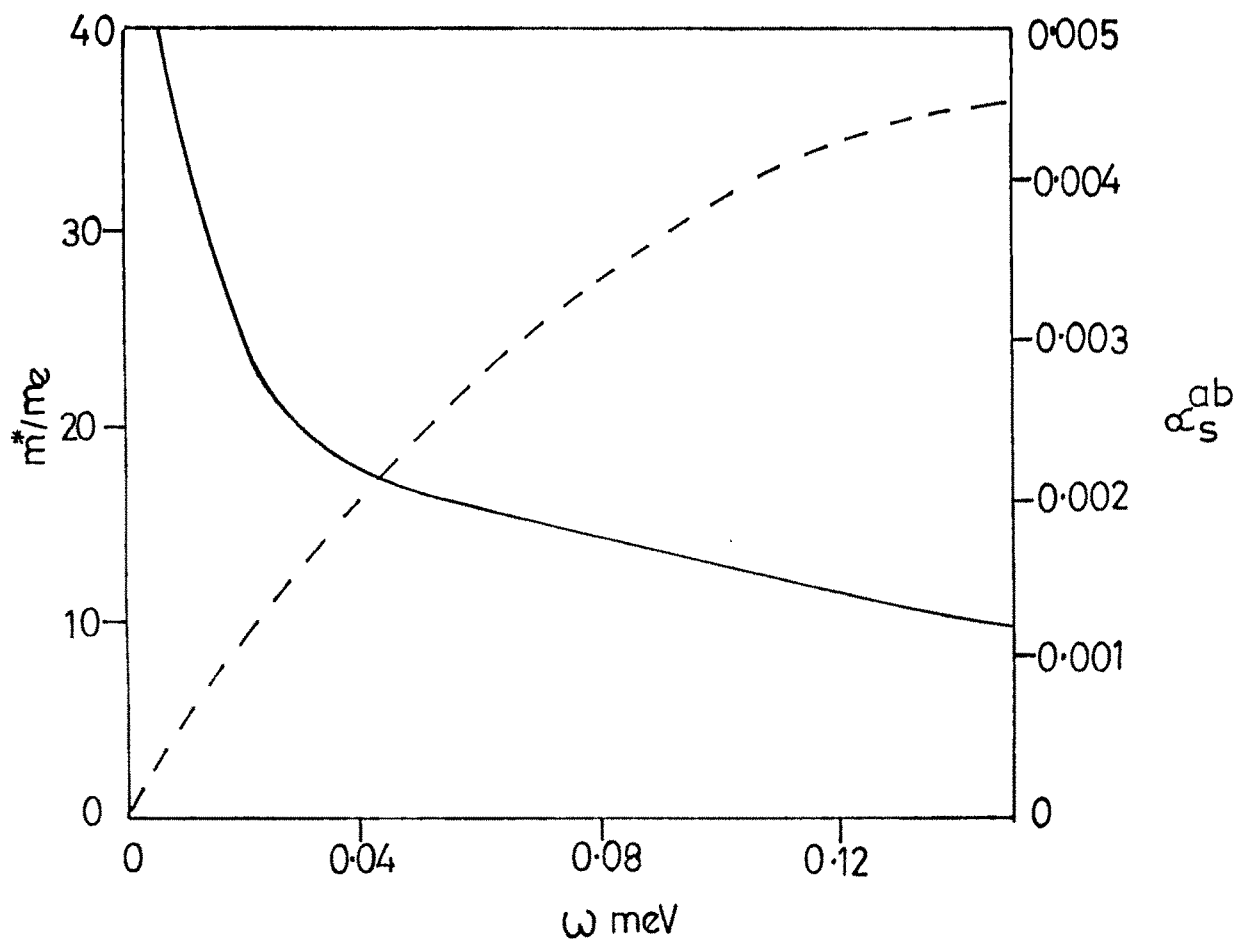
Fig. 3.2 Plot of m^*/m_e versus ω (solid line curve) and $\alpha_s{}^{ab}$ versus ω (desh-desh curve) for $\omega \leq 0.15$ meV.
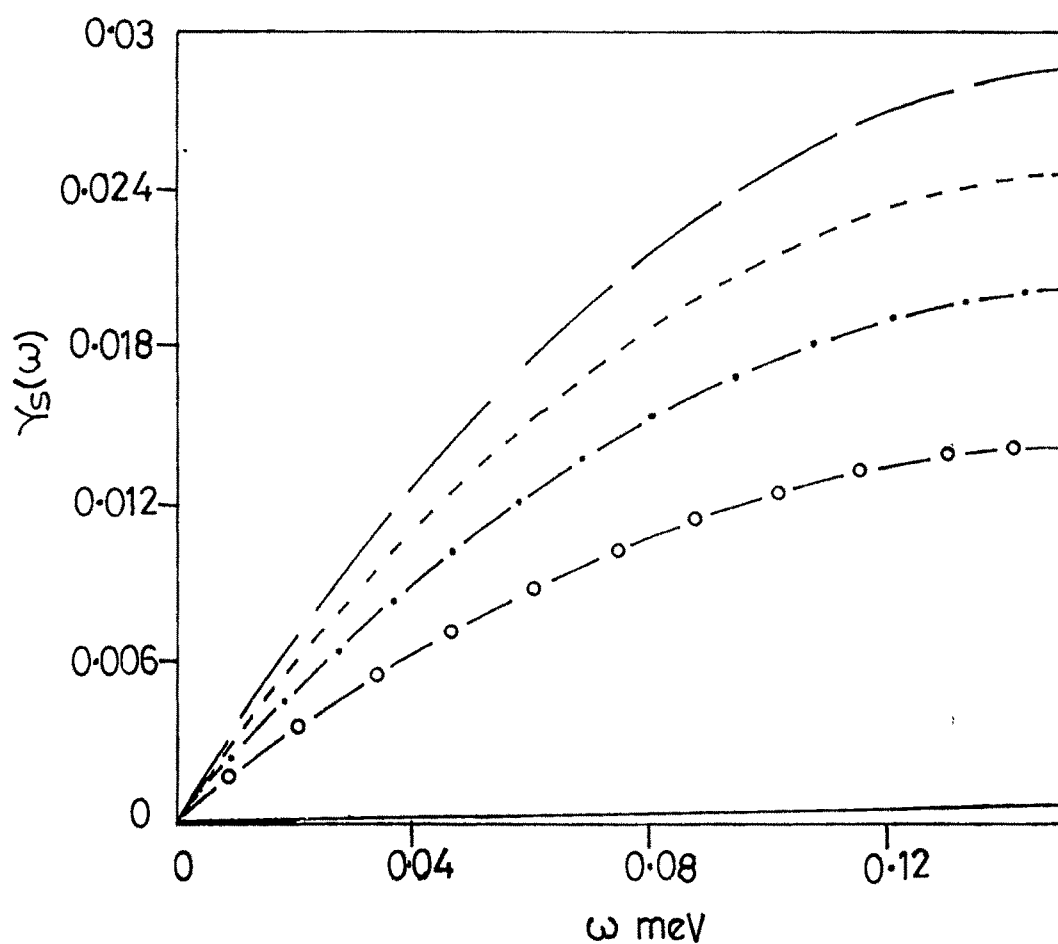
Fig. 3.3 Plot of γ_s versus ω for T=0 K (solid line curve), T=20 K (desh- open circle curve), T=40 K (desh-dot curve), T=60 K (desh-desh curve) and T=80 K (broken line curve).

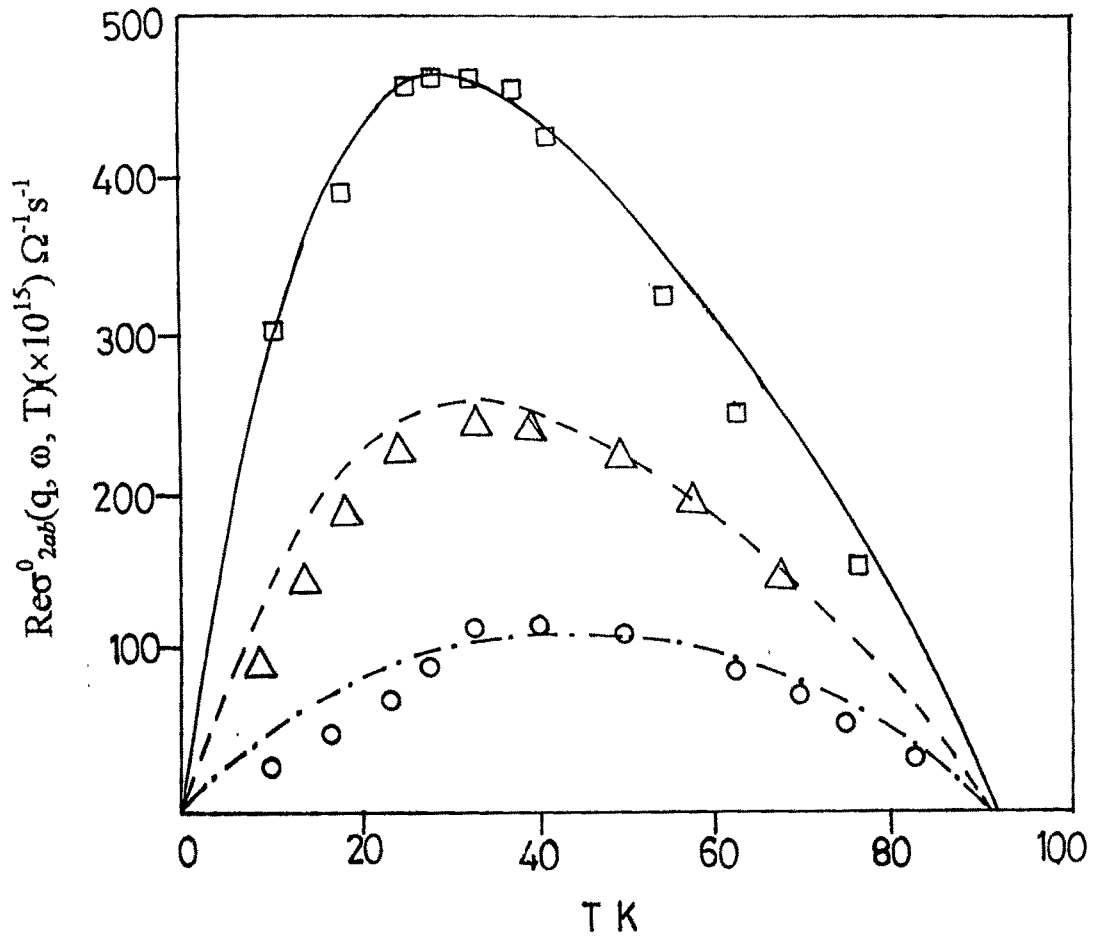**Fig. 3.4** Plot of $Re\sigma^0_{2ab}(q, \omega, T)$ versus T for $\omega=0.0122$ meV (solid-line theo. curve and square expt. data), $\omega = 0\,0397$ meV (desh-desh, theo. curve and triangles expt. data) and $\omega=0.144$ meV (desh-dot theo. curve and open circle expt. data) at $qd=1\times10^{-7}$.Experimental data is taken from Ref. 4,3 and 2.

results, we used $\beta_n^{ab} = 0.4$ meV/K, $\beta_s^{ab} = 0.5$ meV/K, $\alpha_n^{ab} = 0.55$. The superscript *ab* is used to identify the value of parameters for *a-b* plane. The guiding principle to choose these values of parameters has been the best possible agreement between our calculations and experimental results. We found that T-dependence of $Re\sigma^0_{2ab}(q, \omega, T)$ comes from the T-dependence of $\gamma_s^{ab}(\omega, T)$, $\gamma_n^{ab}(\omega, T)$ and of X_s. It has further been found that the peak in our computed $Re\sigma^0_{2ab}(q, \omega, T)$ cannot be seen on taking; (i) T-independent value of γ_s^{ab} and (ii) qv_F close to $|\omega + i\gamma_s^{ab}|$. This suggest that to understand the experimentally observed peak in microwave conductivity (as a function of temperature below T_c) within the frame-work of Fermi-liquid theory, one has to take ω and T dependent transport relaxation time. During the computation of our results, we found that; (i) height of peak in $Re\sigma^0_{2ab}(q, \omega, T)$ is basically governed by ω_p and (ii) position and shape of peak is controlled by the choice of values of β_s^{ab} and α_s^{ab}. On increasing β_s^{ab} and keeping α_s^{ab}, β_n^{ab}, α_n^{ab} and m^*/m_e unchanged, peak height increases and peak position shifts towards lower value of ω. We further found that the T-dependence of $Re\sigma^0_{2ab}(q, \omega, T)$ for T$\leq$peak position remains almost unchanged whereas, $Re\sigma^0_{2ab}(q, \omega, T)$ exhibits stronger T-dependence for T$>$peak position, on increasing β_s^{ab}. As can be seen from Fig. 3.4, $Re\sigma^0_{2ab}(q, \omega, T)$ versus T decreases on increasing ω when other parameters remains unchanged. The figure clearly shows that model calculation gives a very good agreement with experimental results for appropriate choice of parameters used in our calculation.

We computed $Re\sigma^0_{2c}(k_z, \omega, T)$, real part of $\sigma^0_{2c}(q, k_z, \omega, T)$ along *c*-axis as a function of T for $\omega=0.0397$ meV and $k_z d \ll 1$ ($k_z d = 1 \times 10^{-6}$). Values of rest of the parameters are taken as follows: $\beta_s^c = 5000.0$ meVK, $\alpha_s^c = 0.00027$, $\beta_n^c = 4000.0$ meVK, $\alpha_n^c = 0.11$, $\omega_g = 98.85$ meV and $\omega_p = 312.62$ meV. For computation of $Re\sigma_{2c}^0(k_z, \omega, T)$ as a function of T at one value of ω, we do not

require a curve between α_s^c and ω. Our computed $Re\sigma^0_{2c}(k_z, \omega, T)$ is plotted as a function of T in Fig. 3.5, along with experimental results from Ref. 2. As can be seen from the figure our calculated $Re\sigma^0_{2c}(k_z, \omega, T)$, gives a good agreement with experimental results. Agreement between theory and experiment is much better for T≤peak position as compared that for T>peak position. It is to mentioned that in computation of $Re\sigma^0_{2ab}(q, \omega, T)$ and $Re\sigma^0_{2c}(k_z, \omega, T)$,, we used ω-dependent and T-independent m^*. However, it has been suggested that a T-dependent m^* can be used to improve further the agreement between theory and experiment [28]. Therefore it is possible to obtain excellent agreement between our calculation and experimental data on microwave $Re\sigma^0_{2ab}(q, \omega, T)$ and $Re\sigma^0_{2c}(k_z, \omega, T)$ by considering ω-and T-dependence of both m^* and γ_s along with right choice of values of other parameters involved in our calculation. An important point which very clearly emerges from our work is ω- and T-dependence of γ_s and γ_n in the form similar to our Eq. (3.14) is to be taken.

Our computed $Re\sigma^0_{2ab}(q, \omega, T)$ as a function of ω at T=20 K and qd=1×10^{-7} is plotted in Fig. 3.6, along with experimental data from Ref. 30. For computation of $Re\sigma^0_{2ab}(q, \omega, T)$, we used α_s^{ab} and m^*/m_e given by Eq. (3.15) and (3.16) for $\omega\leq0.15$ meV, whereas for $\omega>0.15$ meV, we used α_s^{ab}=0.05 and m^*/m_e=2.0. The values of the rest of the parameters are taken those used to compute $Re\sigma^0_{2ab}(q, \omega, T)$ as a function of T. We compute $Re\sigma^0_{2ab}(q, \omega, T)$ versus ω for the range of ω for which experimental data has been reported [30]. As is seen from the figure, our calculation shows a good agreement with experimental results for $\omega\leq400$ cm^{-1}. The small-small peaks appearing in lower range of ω of experimental results belong to lattice vibrations. These peaks are also seen in our computed results on $Re\sigma^0_{2ab}(q, \omega, T)$ as a function of ω. For larger value of ω ($\omega\geq400$ cm^{-1}) our computed results shows large discrepancy
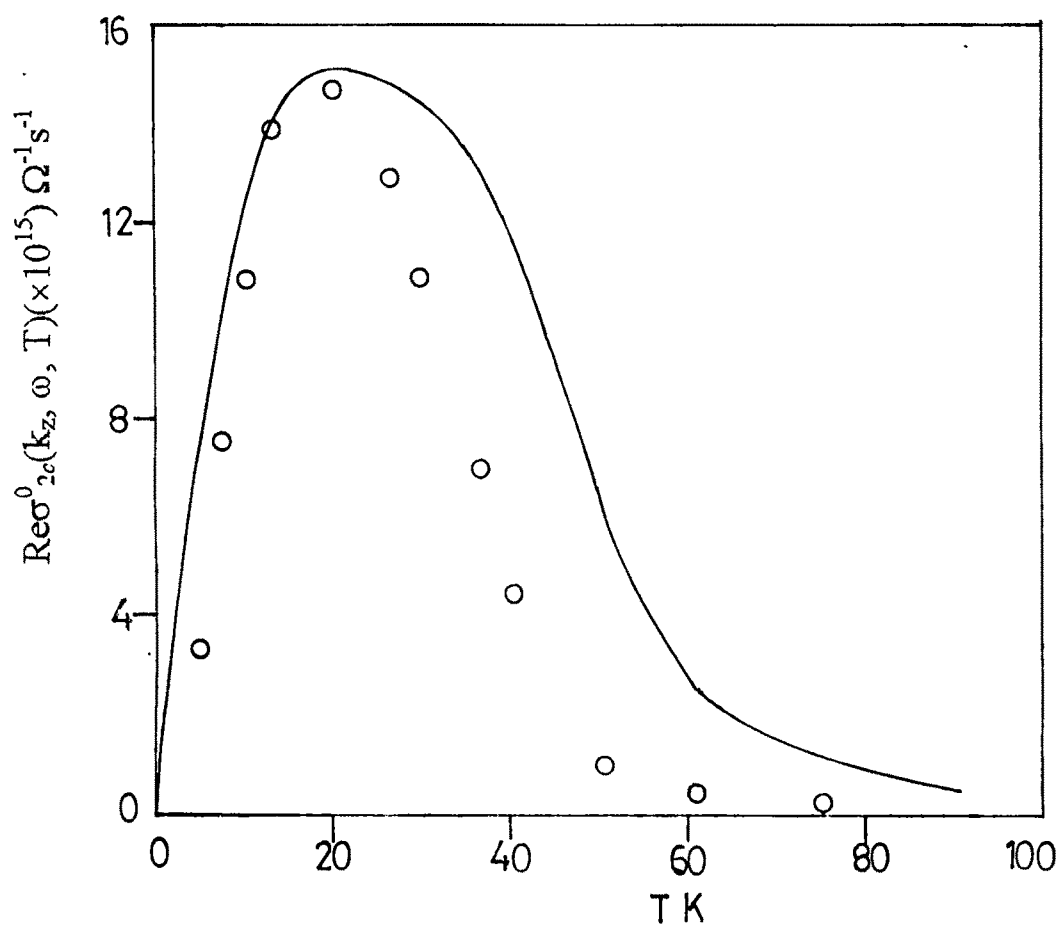
Fig. 3.5 Plot of $Re\sigma^0_{2c}(k_z, \omega, T)$ versus T for $\omega=0.0122$ meV (solid-line curve), $\omega=0.0397$ meV at $k_zd=1\times10^{-6}$ along with experimental data from Ref. 3.
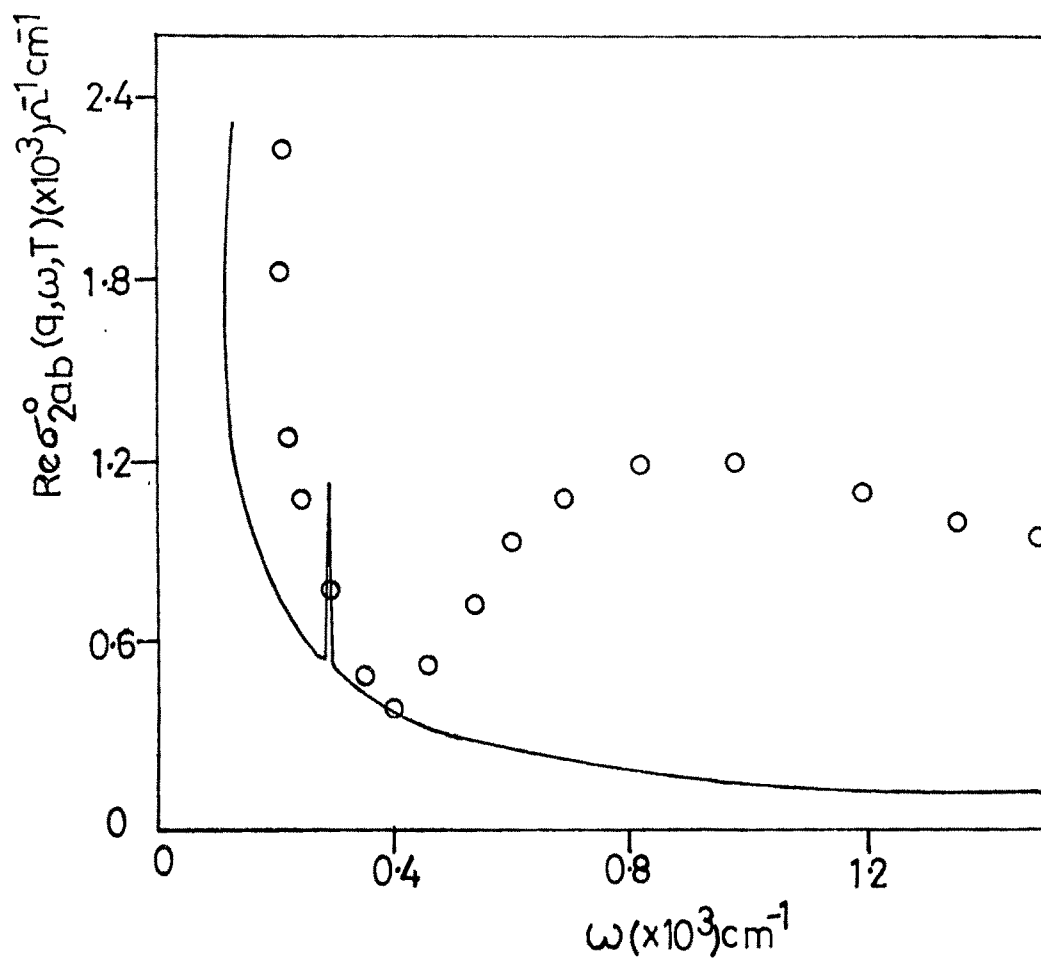
Fig. 3.6 Plot of $Re\sigma^0_{2ab}(q, \omega, T)$ versus ω at T=20 K and qd=1×10^{-7} along with experimental data from Ref. 30.

with experimental data. It has been suggested that for larger value of ω (frequency is much larger than the frequency of lattice modes), transition between different bonds significantly contributes to ω-dependent conductivity. As our calculation does not incorporate interband transition, large discrepancy between our calculation and experimental results is expected in a manner.

As can be seen from the Eq. (3.9), $\sigma_2^0(q, k_z, \omega, T)$ is contributed by both intralayer as well as interlayer interactions, whereas $\sigma_1^0(q, k_z, \omega, T)$ is contributed by intralayer interactions only. We have computed intralayer contribution and interlayer contribution to $Re\sigma_2^0(q, k_z, \omega, T)$ separately as a function of T at fixed ω-values and then as a function of ω at fixed value of T. We found that interlayer interaction contribution more for smaller value of ω and T and their contribution is positive. However for $qd \ll 1$ and $k_z d \ll 1$, contribution from interlayer interactions to $Re\sigma_2^0(q, k_z, \omega, T)$ is negligibly small as compared that from intralayer interactions. Because of this reason, behavior of our computed $Re\sigma_{1ab}^0(q, \omega, T)$ and $Re\sigma_{1c}^0(k_z, \omega, T)$, versus T at fixed ω-value and as a function of ω at fixed T-value, found very similar to that of $Re\sigma_{2ab}^0(q, \omega, T)$ and $Re\sigma_{2c}^0(k_z, \omega, T)$, respectively. $Re\sigma_{1ab}^0(q, \omega, T)$ and $Re\sigma_{1c}^0(k_z, \omega, T)$ are the real parts of $\sigma_1^0(q, k_z, \omega, T)$ along a-b plane and along c-axis, respectively. We therefore do not report our discussion on $Re\sigma_{1ab}^0(q, \omega, T)$ and $Re\sigma_{1c}^0(k_z, \omega, T)$.

3.3.1(b) Microscopic Conductivity

The most interesting part of our study of $\sigma_2(q, k_z, \omega, T)$ and $\sigma_1(q, k_z, \omega, T)$, which are given by Eq. (3.5), is the peaks in $Re\sigma_2(q, k_z, \omega, T)$. The peaks in $Re\sigma_2(q, k_z, \omega, T)$ corresponds to zeros of the $\varepsilon_2(q, k_z, \omega, T)$. Solution of $\varepsilon_2(q, k_z, \omega, T)=0$ for ω as a function of q, k_z and T gives the

frequency of collective excitation modes (plasmons) in the system. A collective state appears in CS at different frequency-values which are determined by q, k_z and T. The frequency for collective state can also be determined by computing $Im\{-1/\varepsilon_2(q, k_z, \omega, T)\}$ as a function of T for different values of q, k_z and ω. Our computed $Im\{-1/\varepsilon_{2ab}(q, \omega, T)\}$ as a function of ω is plotted in Fig. 3.7, at two values of T (40 K and 20 K) for $qd=1\times10^{-7}$. The $\varepsilon_{2ab}(q, \omega, T)$ is the value of $\varepsilon_2(q, k_z, \omega, T)$ along a-b plane. Figure-3.7 shows a broad peak for ω close to ω_p. Both unpaired electron (represented by X_n) and paired electron (represented by X_s) contribute to collective state of CS. The broadness of peak in Im $\{-1/\varepsilon_{2ab}(q, \omega, T)\}$ is the indication of large contribution from unpaired electrons along a-b plane. It is interesting to notice that change in temperature does affect much the frequency of a collective state. Figure also shows a small and sharp peak in lower region of ω-values. This peak represents the collective state which basically belong to lattice vibrations (phonons). We also computed $Im\{-1/\varepsilon_{2c}(k_z, \omega, T)\}$ as a function of ω for $k_zd=1\times10^{-6}$ and T=40 K. Similar to the case of $Im\{-1/\varepsilon_{2ab}(q, \omega, T)\}$, $Im\{-1/\varepsilon_{2c}(k_z, \omega, T)\}$ also shows one broader and large peak which appears at ω close to ω_g and two smaller peaks appearing in the range of ω for $\omega\leq20$ meV. The large peak represents electronic collective excitations, whereas smaller peaks represents lattice vibration.

The collective state which corresponds to zeros of $\varepsilon_2(q, k_z, \omega, T)$ can also be study by plotting $Im\{-1/\varepsilon_{2ab}(q, \omega, T)\}$ as a function of T for fixed value of ω and qd. Our computed $Im\{-1/\varepsilon_{2ab}(q, \omega, T)\}$ is plotted as a function of T for three different value of ω (0.0122 meV, 0.0397 meV and 0.144 meV) in Fig. 3.8. A doublet in $Im\{-1/\varepsilon_{2ab}(q, k_z, \omega, T)\}$ versus T can be seen for T varying in the range of 82 K to 85 K. It is important to notice that the position of the peaks does not change while height of the peak increases on increasing ω.
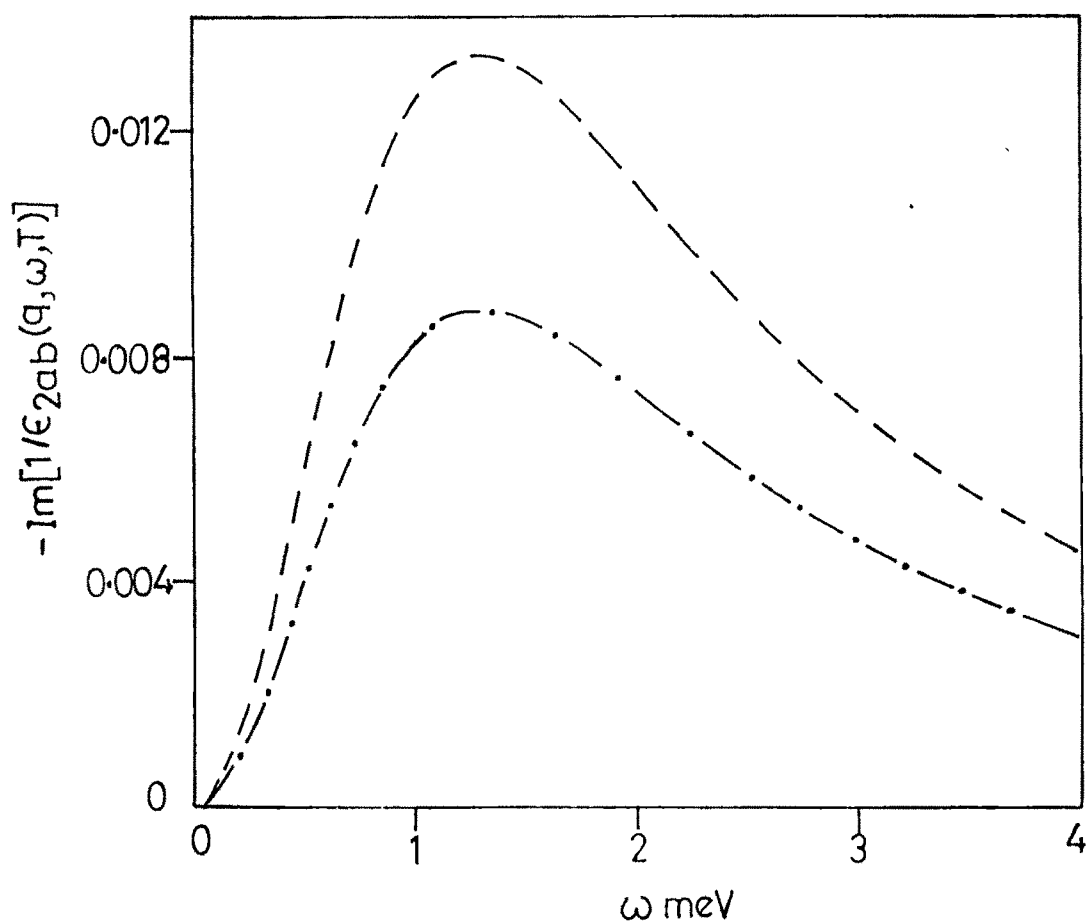
Fig. 3.7 Plot of $-\mathrm{Im}\{1/\epsilon_{2ab}(q, \omega, T)\}$ versus ω at T=20 K (desh-dot curve) and T=40 K (desh-desh curve) for $qd=1\times10^{-7}$.
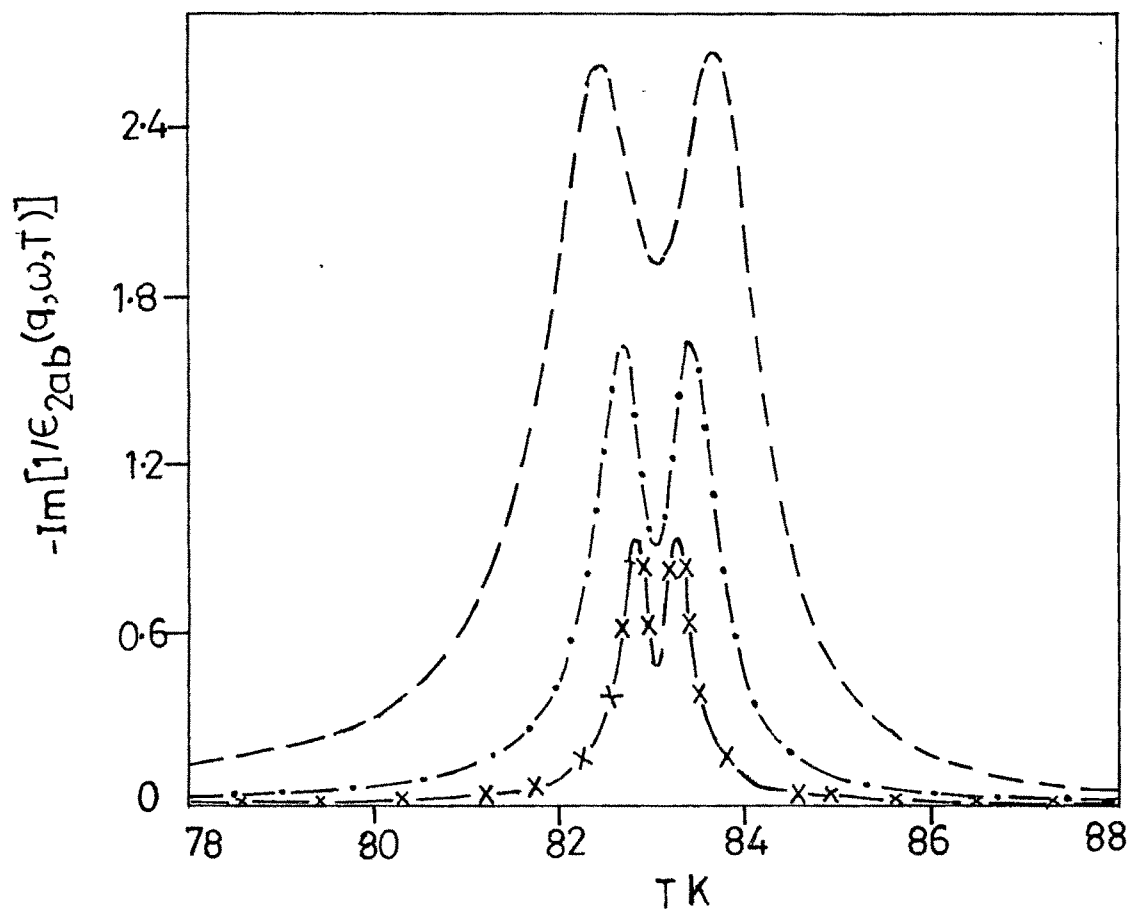
Fig. 3.8 Plot of $-\mathrm{Im}\{1/\varepsilon_{2ab}(q, \omega, T)\}$ versus T for $\omega = 0.0122$ meV (cross-desh curve), $\omega = 0.0397$ meV (desh-dot curve) and $\omega = 0.144$ meV (desh-desh curve) at $qd = 1 \times 10^{-7}$.

In order to study the propagation of an electronic collective excitations mode along an arbitrary direction, we computed the zeros of $\varepsilon_2(q, k_z, \omega, T)$ as a function of qd for three values of $k_z d$ (0.01 0.05 and 0.1) at T= 20 K, taking ε_l = 4.0 (independent of ω). Our computed results are plottted in Fig. 3.9. As can be seen from figure frequency of a collective excitation mode is smaller than superconducting gap (2Δ= 20.895 meV) and it exhibits a linear dependence on qd. The general behavior of frequency of our computed collective excitation mode as a function of wave vector is very similar to the behavior of collective mode spectrum in asuperconducting superlattice, which has been reported by Fertig and Das Sarme [23]. On looking at Fig. 3.7 and 3.9, we notice that to observe soft collective excitation mode, which are plotted in Fig. 3.9, both qd and $k_z d$ should be non-zero and comparable with each other. For qd→0 and $k_z d$→0, these collective excitation modes disappears because of pair breaking effect and a collective state appears at frequency close to ω_p.

3.4 CONDUCTIVITY WHEN NO CHARGE TRANSFER BETWEEN CONDUCTING LAYERS

In order to study collective excitations for temperature just below T_c, Sharma and Kulshreshtha [31] calculated polarizability for CS by modelling them as layered electron gas (LEG), where charge transfer between the conducting layers is not allowed. The P(q, ω, T) {= $(2\pi e^2/q)$ $\Pi(q, \omega, T)$)} is given by [31,32]

$$P(q, \omega, T) = (2/q \, a^*) \left[1 - \left\{ \frac{\Delta}{2T} \cdot \frac{\omega}{qv_F} \left(1 - \frac{\Delta}{2T} \right) \right\} \right] + \frac{\omega_p^2}{Aq^2(4\Delta^2 - \omega^2)^{1/2} - \omega^2},$$
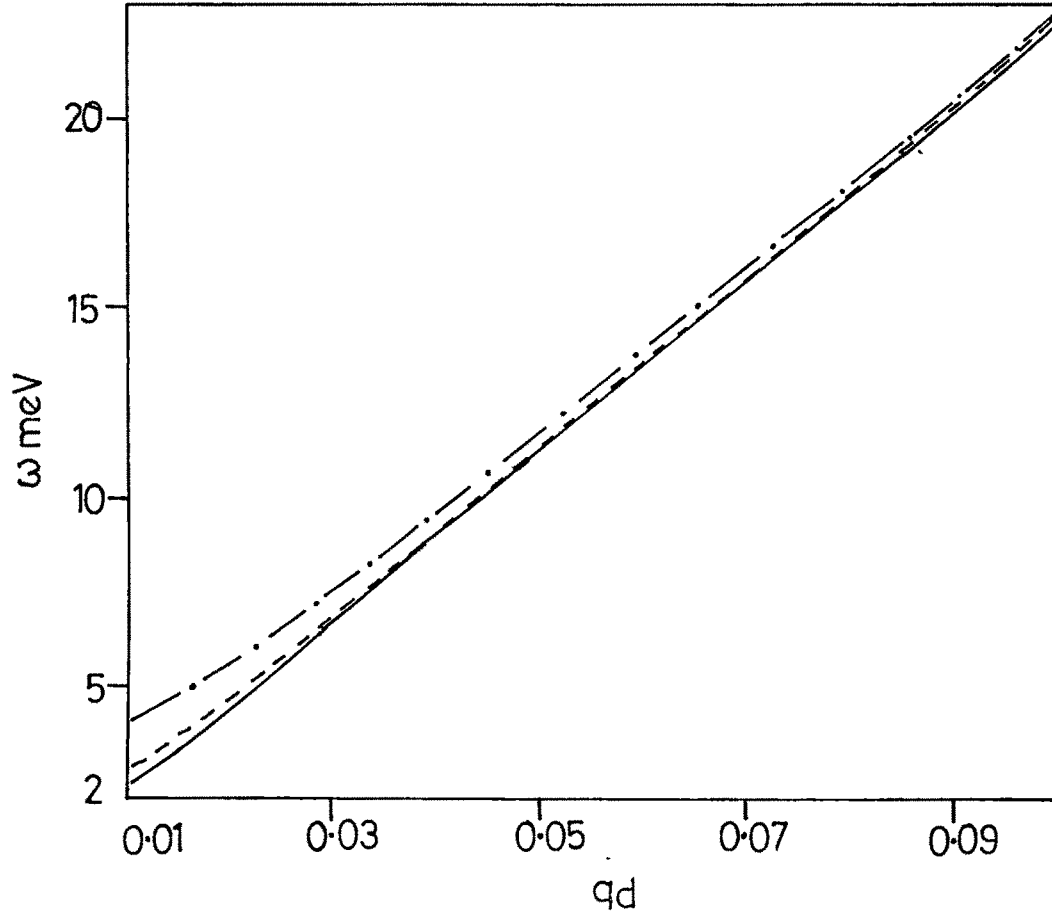
(3.17)

76

Fig. 3.9 Plot of frequency (ω) of collective excitation modes versus qd at $k_zd=0.01$ (solid-line curve). $k_zd=0.05$ (desh-desh curve) and $k_zd=0.1$ (desh-dot curve) at T=20 K.

where $a^* = \hbar^2 \varepsilon_0 / m^* e^2$ is the effective Bohr radius, $\omega_p = (2\pi n_2 e^2 q / m^* \varepsilon_0)$ is the usual plasma frequency of a 2D electron gas and n_2 is number of electrons per unit area. The parameter A is defined to be

$$A = (n_s/n_2)(v_F^2 T/2\Delta^2). \qquad (3.18)$$

(n_s/n_2) represents the fraction of superfluid $n_2 = n_s + n_n$ is number of superconducting electrons which varies with T_c and n_n is number of normal electrons per unit area. An emperical relation based on the two-fluid model has been used to describe the T-dependence of (n_s/n_2) [32]

$$n_s/n_2 = [1 - (T/T_c)^4]. \qquad (3.19)$$

The T-dependence of A is taken from the experimental results of Ekino and Akimistu [33]. We used the emperical relation

$$T/T_c = \frac{\Delta/\Delta_0}{\tanh^{-1}(\Delta/\Delta_0)} \qquad (3.20)$$

which reproduces the experimental results [33] for $\Delta_0 = 3k_B T_c$. Eq. (3.17) has two terms on right hand side. First term represents the normal electrons, whereas second term is contributed by paired electrons (superelectrons). In absence of impurity scattering, single particle excitations in normal fluid causes damping of collective excitations of paired electrons. Damping of collective excitations of paired electrons also occured due to electron impurity scattering. The impurity scattering is incorporated in a phenomenological manner in our calculation by replacing ω^2 by $\omega(\omega+i\gamma)$, where γ is single particle damping.

Strictly speaking Eq. (3.17) is valid in the frequency range $\hbar\omega \leq 2\Delta < qv_F < k_\beta T < k_\beta T_c$, where q, Δ, v_F, k_β and T are the components of the wave vector in the *a-b* plane, the binding energy of Cooper-pair, Fermi velocity, Boltzman's constant and temperature, respectively. We calculated $\sigma_1^0(q, k_z, \omega, T)$, $\sigma_2^0(q, k_z, \omega, T)$, $\sigma_1(q, k_z, \omega, T)$ and $\sigma_2(q, k_z, \omega, T)$ using Eq. (3.17) in Eqs. (3.5) to (3.10). In order to calculate dynamical conductivity of a conducting layer in our model system, we performed averaging over k_z in following manner

$$\sigma_\rho(q, \omega, T) = d/2\pi \int_{-\pi/d}^{\pi/d} \sigma_\rho(q, k_z, \omega, T) \, dk_z \qquad (3.21)$$

Further averaging can be made over q to obtain $\sigma_\rho^0(\omega, T)$ and $\sigma_\rho(\omega, T)$.

The inverse transport relaxation time (γ_s) can approximately be estimated using [34]

$$\gamma_s = \frac{\omega \, \sigma_\rho'(\omega, T)}{\sigma_\rho''(\omega, T)} \qquad (3.22)$$

and surface impedance can be obtain from [35]

$$Z(\omega, T) = \left| \frac{i\omega}{4\pi\sigma_\rho(\omega, T)} \right|^{1/2}, \qquad (3.23)$$

where $\sigma_\rho'(q, \omega, T)$ and $\sigma_\rho''(\omega, T)$ are the real and imaginary part of $\sigma_\rho(\omega, T)$.

78

3.4.1 RESULTS AND DISCUSSION

We computed our results of this section for $La_{2-x}Sr_xCuO_4$ by modelling it in terms of following values of parameters: $m^*=3.5m_e$, $n_2=1.277\times10^{14}$ cm^{-2}, $d=13.25$ A^0 and $v_F=0.9414\times10^7$ cm s^{-1}. Figure 3.10 shows plot of $\sigma'_1(\omega, T)$ and $\sigma''_1(\omega, T)$ as a function of ω for both the cases of with and witout including impurity scattering. It is seen from the figure that on inclusion of impurity scattering the peak height of $\sigma'(\omega, T)$ drastically reduces by an order of 10^3 and becomes much broader as compared to that in $\sigma'_1(\omega, T)$ without impurrity scattering. The general behavior of $\sigma'_1(\omega, T)$, including impurity scattering, as a function of ω is very similar to that of $Re\sigma_{1ab}(q, \omega, T)$ versus ω, which has been computed in sec. 3.3. Whereas it is almost insignificant for frequencies which are not close to pasma frequency. Also it can be seen that the two curves of the $\sigma''_1(\omega)$ versus ω (i.e. curves with and without including impurity scattering) coincide with each other. The position of peak $\sigma'_1(\omega, T)$ represents plasma frequency of our model $La_{2-x}Sr_xCuO_4$ at $T/T_c=0.997$ (just below T_c).

Figure 3.11 shows the plot of $\omega(\sigma'_1/\sigma''_1)$ versus ω for $T/T_c=0.997$. The $\omega(\sigma'_1/\sigma''_1)$ yields an approximate estimate of γ_s. It can be seen from figure that $\omega(\sigma'_1/\sigma''_1)$ exhibits almost linear ω-dependence for $\omega\leq0.8$ meV. As has been discussed in sec. 3.3, linear ω-dependence of γ_s is characteristics of quasi-two dimensional charge carriers which exist in a CS. This justifies our choice of ω-dependence of γ_s which is givn by Eq. (3.14). Our computed $R_s(\omega)$ (real part of $Z(\omega)$) is plotted as a function of ω at $T/T_c=0.997$ in Fig. 3.12 for both the cases of with and without impurity scattering. The $R_s(\omega)$ shows a sudden change at frequencies near to plasma frequency. The sudden change in $R_s(\omega)$ represents the collective excitation state of system, which exists in our model system just below T_c. The change becomes smoother on inclusion of impurity scattering in
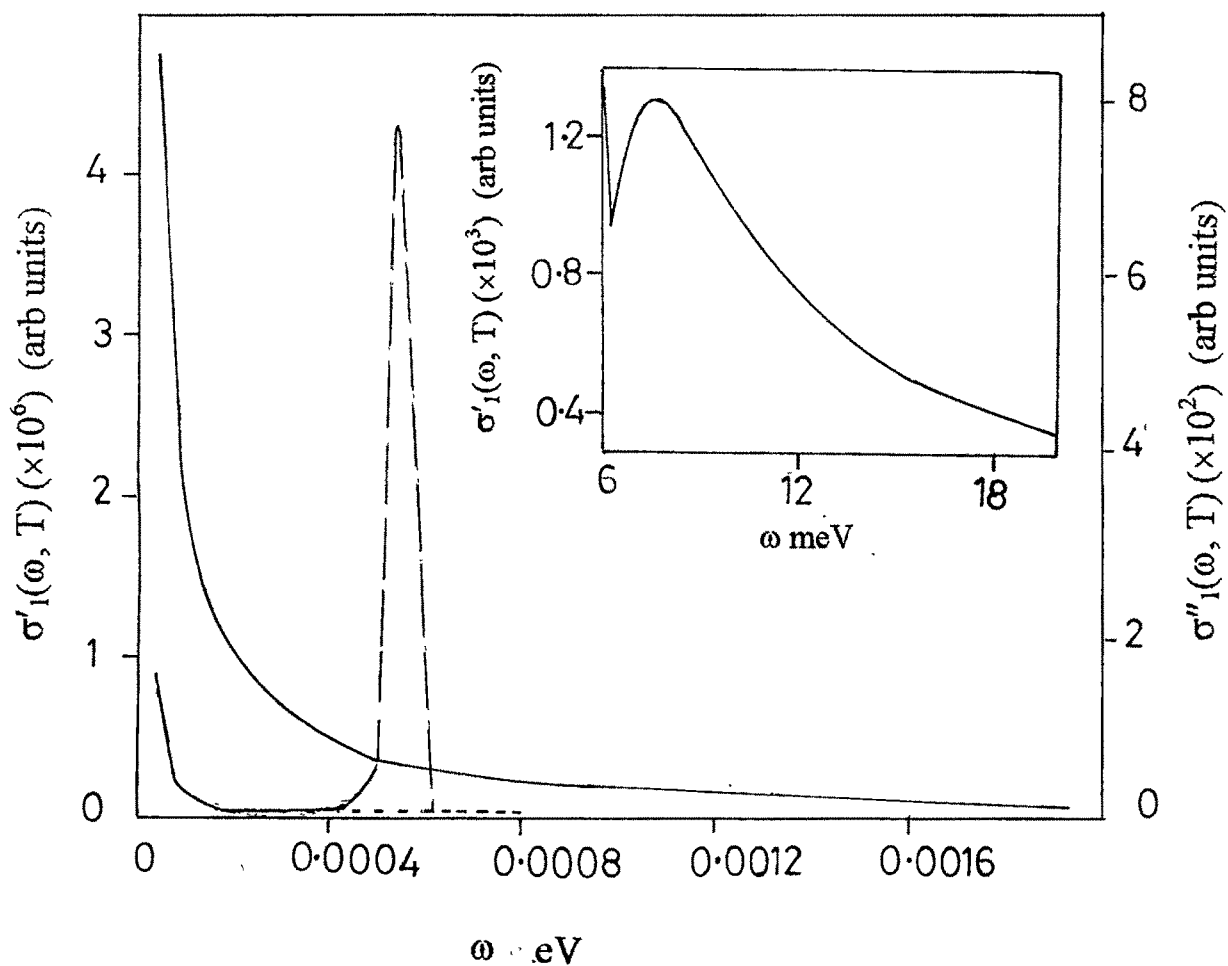
Fig. 3.10 Plot of $\sigma'_1(\omega, T)$ and $\sigma''_1(\omega, T)$ versus ω at $T/T_c=0.997$. Without impurity scattering: large desh-desh curve (σ'_1) and solid line curve (σ''_1). With impurity scattering: inset curve (σ'_1) and small desh curve (σ''_1).
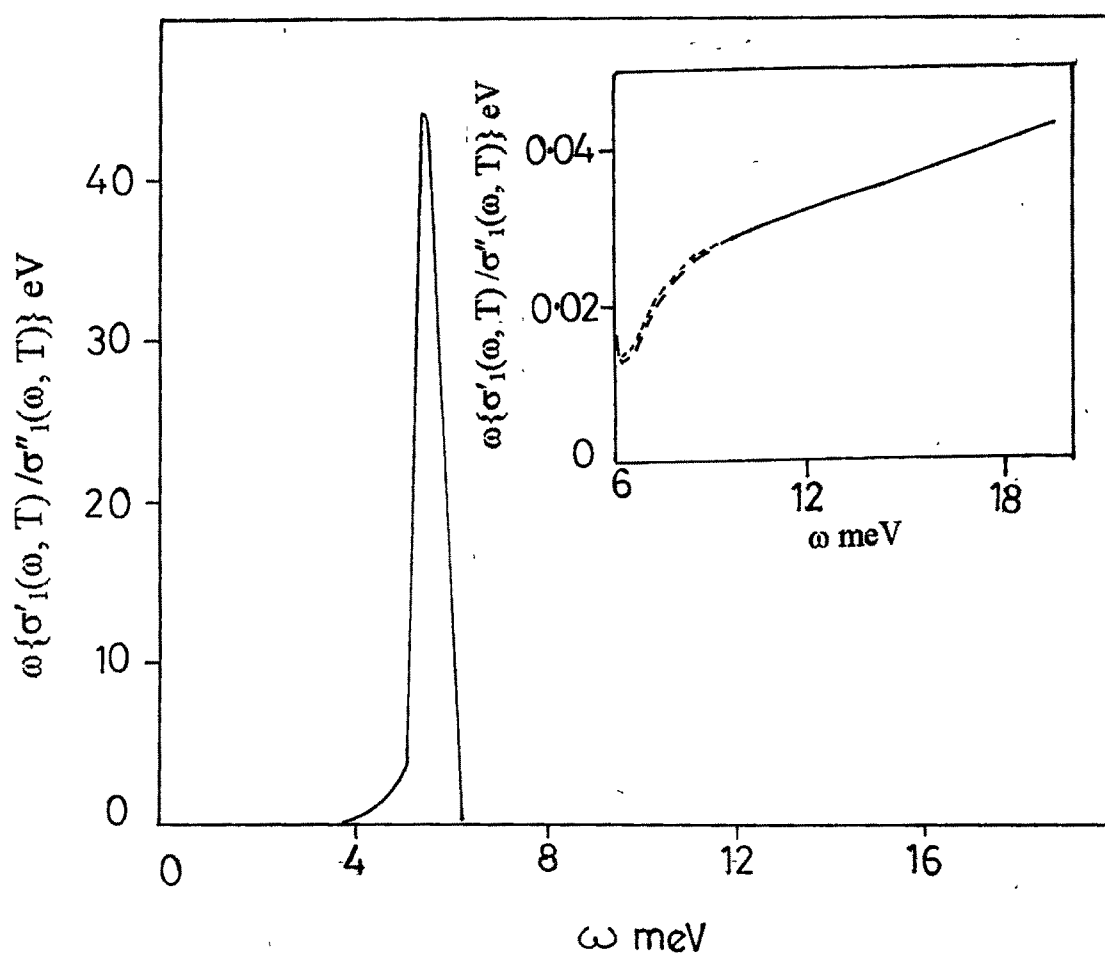
Fig. 3.11 Plot of $\omega\{\sigma'_1(\omega, T)/\sigma''_1(\omega, T)\}$ versus ω at $T/T_c=0.997$. Inset curve. Inset curve with impurity scattering (desh-desh) and without impurity scattering (solid line curve)
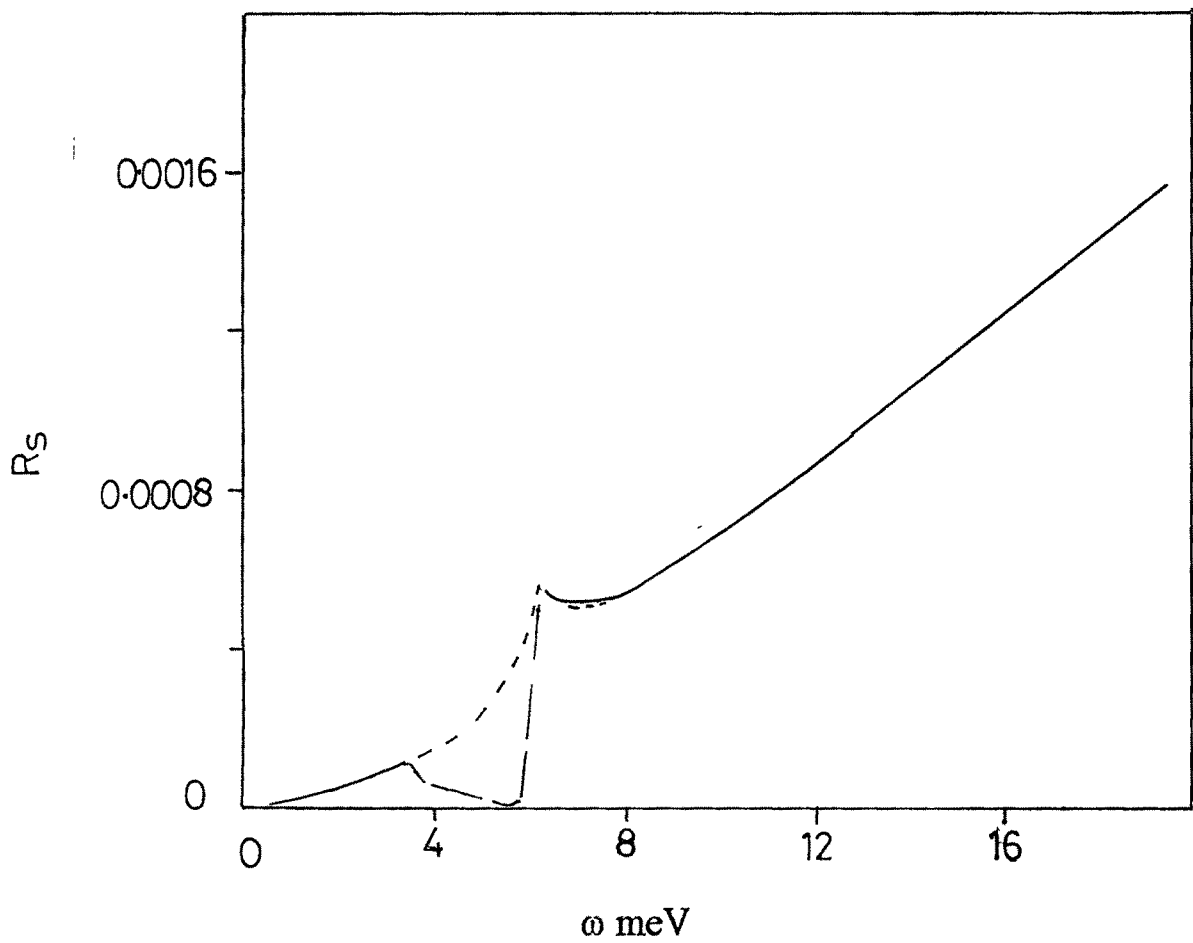
Fig. 3.12 Plot of surface resistance (R_s) versus ω at T/T_c =0.997. With impurity scattering (desh-desh curve) and without impurity scattering scattering (solid line curve).

$\sigma_1(\omega, T)$. Also, $R_s(\omega)$ almost linearly increases with ω for $\omega>0.8$ meV, which agree with the work of Chang et. al.[35]. The aim of calculation presented in this section has been to calculate dynamical conductivity by making use of our earlier model calculation of polarizability and to show that both types of polarizabilities result in a similar conclusion.

REFERENCES

[1]. D. N. Basov et. al., **Phys. Rev. Lett. 74** (1995), 598.

[2]. D. A. Bonn, S. Kamal, S. Zhang, R. Liang, D. J. Baar, E. Klein and W. N. Hardy, **Phys. Rev. B50** (1994), 4051.

[3]. Jian Mao, D. H. Wu, J. L. Peng, R. L. Greene and Steven M. Anlage, **Phy. Rev. B51** (1995), 3316.

[4]. D. A. Bonn, P. Dosanjh, R. Liang, and W.N. Hardy, **Phy. Rev. Lett. 68,** (1992), 2399.

[5]. W. N. Hardy, D. A. Bonn, D.C. Morgan, Ruixing Liang and Kuan Zhang, **Phys. Rev. Lett. 70** (1993), 3999.

[6]. A. A. Tsvetkov et.al., **Phys. Rev. B55** (1997), 14152.

[7]. A. Pimenov, A. Loidl, G. Jakob and H. Adrian, **Phys. Rev. B59** (1999), 4390.

[8]. Shih-Fu Lee, D. C. Morgan, R. J. Ormeno, D. M. Broun, R. A. Doyle and J. R. Waldram, **Phys. Rev. Lett. 77** (1996),735.

[9]. D. M. Broun, D. C. Morgan, R. J. Ormeno, S. F. Lee, A. W. Tyler, A. P. Meckenzie and J. R. Waldram, **Phys. Rev. B56** (1997), R11443.

[10]. R. Hlubina. Phys. Rev. B58 (1998), 8240.

[11]. P. J. Hirschefeld, W. O. Putikka and D. J. Scalapino, **Phys. Rev. Lett. 71** (1993), 3705.

[12]. C. A. Hayward, D. Poilbanc and D. J. Scalapino, **Phys. Rev. B53** (1996), R8863.

[13]. B. P. Stojkovic and D. Pines, **Phys. Rev. B56** (1997), 11931.

[14]. W. A. Atkinson and J. P. Carbotte, **Phy. Rev. B52** (1995), 10601.

[15]. C. Jiang and J. P. Carbotte, **Phys. Rev. B53** (1996), 12400.

[16]. W. A. Atkinson and J. P. Carbotte, **Phy. Rev. B55** (1997), 12748.

[17]. Hae-Youhg Kee and Jongboe Hong, **Phys. Rev. B55** (1997), 5670.

[18]. H. Kitano, T. Hanaguri and A. Maeda, **Phy.Rev. B57** (1998),10946.

[19]. D. Mihalovie, T. Merteli and K. A. Muller, **Phy. Rev. B57** (1996),6116 and references therein.

[20]. P. W. Anderson, "*The Theory of Superconductivity in the High-T_c Superconductors*" (Princeton University Press, Prienceton, 1997).

[21]. A. V. Chubukov, D. Pines and B. P. Stojkovic, **J. Phys, Condens Matt. 8**, (1996),10017, J. R. Schrieffer and A. P. Kampf, **J. Phys. Chem. Solids 56** (1995), 1673.

[22]. J. Parade, A. D. Kulkarni, F. Wade Wette, W. Kress, M. Cardona, R. Riger and U. Schroder, **Solid State Comm. 64**, (1987),1267.

[23]. H. A. Fertig and S. Das Sarma, **Phys. Rev. B44** (1991), 4480.

[24]. Shih-Fu Lee, D. C. Morgan, R. J. Ormeno, D. M. Broun; R. A. Doyle and J. R. Waldram, **Phys. Rev. Lett.** 77(1996), 735.

[25]. Cui, S-M and Tsai, C-H, **Phys. Rev. B44** (1991), 12500.

[26]. H. Ding, M.R. Norman, T. Yokoya, T. Takeuchi, M. Randeria, J. C. Campuzano, T. Takahashi, T. Mochiku and K. Kndowaki, **Phy.Rev. Lett.** 78(1997),2628.

[27]. J. Demsar, M. Zavrtanik and B. Podovmik, V.I. Dediu and D. Mihalovie, **J. Supercond.** 10 (1997), 455.

[28]. A. Virosztek and Ruvalds, **Phys.Rev. Letts.67** (1991), 1657.

[29]. E. Schachinger and J. P. Carbotte, **Phy. Rev. B57**(1998), 7970.

[30]. S. M. Quinnlan, P. J. Hirschfeld and D. J. Scalapino, **Phys. Rev. B53**(1996), 8575.

[31] A. C. Sharma and Ina Kulshrestha, **Physica C 228** (1994), 224

[32] J. R. Schrieffer, "*Theory of Superconductivity*" (W. A. Benjamin, New York, 1964), p-9.

[33] T. Ekino and J. Akimitsu, **Jpn. J. Appl. Phys. 7** (1991), 260 and references therein

[34] C. G. Jiang, E. Schachinger, J. P. Carbotte, D. Basov and T. Timusk, **Phys. Rev. B54** (1996), 1264.

[35] J. J. Chang and D. J. Scalapino, **Phys. Rev. B40** (1989), 4299.